# Tunable site- and orbital-selective Mott transition and quantum confinement effects in $La_{0.5}Ca_{0.5}MnO_3$ nanoclusters

A. Valli,[1,2] H. Das,[3,4] G. Sangiovanni,[5] T. Saha-Dasgupta,[3] and K. Held[1]

[1]*Institute for Solid State Physics, Vienna University of Technology, 1040 Wien, Austria*

[2]*Democritos National Simulation Center, CNR-IOM and Scuola Internazionale Superiore di Studi Avanzati (SISSA), 34136 Trieste, Italy*

[3]*S. N. Bose National Centre for Basic Sciences, 700098 Kolkata, India*

[4]*School of Applied and Engineering Physics, Cornell University, Ithaca, New York 14853, USA*

[5]*Institute for Theoretical Physics and Astrophysics, University of Würzburg, Am Hubland, 97074 Würzburg, Germany*

(Received 29 April 2015; revised manuscript received 8 September 2015; published 22 September 2015)

We present a dynamical mean-field theory study of the charge and orbital correlations in finite-size $La_{0.5}Ca_{0.5}MnO_3$ (LCMO) nanoclusters. Upon nanostructuring LCMO to clusters of 3 nm diameter, the size reduction induces an insulator-to-metal transition in the high-temperature paramagnetic phase. This is ascribed to the reduction in charge disproportionation between Mn sites with different nominal valence [H. Das *et al.*, Phys. Rev. Lett. **107**, 197202 (2011)]. Here we show that upon further reducing the system size to nanoclusters of a few atoms, quantum confinement effects come into play. These lead to the opposite effect: the nanocluster turns insulating again and the charge disproportionation between Mn sites and the orbital polarization are enhanced. Electron doping by means of external gate voltage on few-atom nanoclusters is found to trigger a site- and orbital-selective Mott transition. Our results suggest that LCMO nanoclusters could be employed for the realization of technological devices, exploiting the proximity to the Mott transition and its control by size and gate voltage.

DOI: 10.1103/PhysRevB.92.115143 PACS number(s): 71.27.+a, 71.10.Fd, 71.30.+h, 75.47.Gk

## I. INTRODUCTION

Research on manganites dates back to the 1950s, when Jonker and van Santen [1] reported the existence of a ferromagnetic metallic phase in mixed crystals of manganese oxides $LaMnO_3$-$CaMnO_3$, $LaMnO_3$-$SrMnO_3$, and $LaMnO_3$-$BaMnO_3$. However, the interest of a wide portion of the scientific community was only raised in the 1990s, due to the experimental observation of a colossal magnetoresistance (CMR) effect [2,3]. Indeed, the relative change in resistivity upon the application of an external magnetic field was much higher than the one observed in artificial magnetic/nonmagnetic multilayer systems: up to 60% at room temperature in thin films [2,4]. Triggering such a CMR, however, requires cooling below the Curie temperature $T_C$ and the application of relatively strong magnetic fields, preventing the technical application of the CMR effect to this day. Alternative routes to achieve CMR have also been followed in mixed valence manganites such as the half-doped $La_{0.5}Ca_{0.5}MnO_3$ (LCMO) [5], which is insulating below 155 K and displays antiferromagnetic and charge order [6], often also accompanied by orbital order. Indeed, the antiferromagnetic insulating state is prone to instabilities. The transition toward a ferromagnetic metallic state can be triggered upon applying a magnetic field [7], doping, biaxial strain, pressure [8], or an electric field [9]. The experiments [10–14] suggest that the destabilization of the charge-orbital order can also be obtained upon size reduction. In fact, it was observed also in $Nd_{1-x}Ca_xMnO_3$ [15,16] and $Sm_{1-x}Ca_xMnO_3$ [17], both at half doping and in asymmetrically doped samples, as well as in $Pr_{0.5}Ca_{0.5}MnO_3$ [18–20] compounds. Nonetheless, there remains some controversy [21] arising from the experimental difficulty of disentangling the effects of size reduction from other effects, such as oxygen nonstoichiometry, disorder, and strain.

On the theoretical side, the effects of size reduction have been studied by density functional theory (DFT) + $U$ [22–24] and DFT + dynamical mean-field theory (DMFT) [22]. The theoretical analysis is in remarkable agreement with the experiments and shows a correlation-driven destabilization of the charge-orbital order in bulk LCMO upon size reduction. This bears the prospects that, for the optimized size, a much smaller magnetic field is sufficient to trigger a CMR, as LCMO nanoclusters can be tuned to the verge of a metal-insulator transition. Hitherto, the DFT+DMFT calculations on this topic, e.g., those reported in Ref. [22], were performed for bulk model systems with *ab initio* parameters. That is, following the DFT calculations for 3 nm clusters, model bulk systems were constructed having the same unit cell volume as well as octahedral distortion as in the core of 3 nm cluster. This way, it was possible to take into account the interplay between strong electronic correlations within DMFT and the structural distortions induced by size reduction, obtained *ab initio* through atomic relaxation within DFT. In this paper, we take a significant step forward, in terms of carrying out nanoscopic DMFT calculations for few-atom nanoclusters with a DFT-derived tight-binding Hamiltonian. This gives us the opportunity to consider the effect of size reduction from bulk to intermediate-sized and few-atom clusters. Our calculations show an interesting evolution from the high-temperature paramagnetic insulating (PI) state in the bulk to a paramagnetic metallic (PM) state in intermediate-sized clusters to reentrant PI solution for few-atom clusters. We also investigate the effects of applied hydrostatic pressure in the bulk, which turns out to have different effects with respect to size reduction. Considering few-atom clusters, we also show that electron doping, through the application of an external gate voltage, drives an unexpected site- and orbital-selective Mott transition.

 

The paper is organized as following. In Sec. II we discuss the model employed for the description of mixed-valence manganites, and we describe the strategy we followed to include structural, finite-size, and many-body effects in the framework of a combined DFT+DMFT approach. In Sec. III we present the DMFT results obtained for LCMO nanoclusters of different size. In particular, in Sec. III A and in Sec. III B we focus on the effects of quantum confinement on the spectral properties and on charge-orbital correlations, while in Sec. III C we explore the effect of electrostatic doping by applying an external gate voltage to the few-atom clusters. Finally, in Sec. IV we present our conclusions.

## II. METHOD: DFT+DMFT APPROACH FOR $La_{0.5}Ca_{0.5}MnO_3$ NANOCLUSTERS

### A. Bulk crystal and electronic structure

Manganites, $R_{1-x}A_xMnO_3$ with $R$ being a trivalent rare-earth-metal element and $A$ a divalent dopant, have a perovskite lattice structure, with the rare-earth atoms at corner positions, the Mn atoms at body-centered positions, and oxygen atoms at the face-centered positions. Depending on the sizes of $R$ and $A$, given by the so-called tolerance factor, the $MnO_6$ octahedra can tilt and rotate reducing the symmetry of the perovskite lattice from cubic to orthorhombic. With nominal oxygen valency $O^{2-}$, in half-doped compounds (i.e., $x = 0.5$) the manganite atoms are in a mixed valent $Mn^{3.5+}$ state. This can lead to a charge disproportionation between the Mn sites in bulk half-doped manganites; in the extreme case one has a 50% of $Mn^{4+}$ sites with a $3d^3$ configuration, and the other 50% of $Mn^{3+}$ sites with a $3d^4$ configuration. The charge-ordered state is associated with a real-space ordering of $Mn^{3+}/Mn^{4+}$ species in a 1:1 pattern.

The octahedral crystal field surrounding the Mn ions splits the $3d$ orbitals into three low-energy $t_{2g}$ orbitals ($d_{xy}$, $d_{xz}$, and $d_{yz}$) and two higher-energy $e_g$ orbitals ($d_{3z^2-r^2}$ and $d_{x^2-y^2}$). Due to the strong Hund's exchange coupling, the three Mn electrons of $Mn^{4+}$ occupy the $t_{2g}$ orbital, in a high-spin $S_{t2g} = 3/2$ configuration. The consequent energy gain associated to this state makes it energetically favorable for the extra electron of $Mn^{3+}$ to occupy the doubly degenerate $e_g$ states. Hence, the charge ordering accommodates a static Jahn-Teller distortion at the $Mn^{3+}$ sites, removing the degeneracy and lowering the symmetry of the system to monoclinic. The Mn $e_g$ orbitals are delocalized due to a strong hybridization with the O$2p$ states. On the contrary, Mn $t_{2g}$ orbitals do not hybridize strongly with the O and are localized. The magnetism is thus governed by the double-exchange mechanism [25].

In the half-doped compound, the bulk monoclinic unit cell of LCMO contains eight Mn atoms but only three kinds of Mn atoms are locally inequivalent, labeled as Mn1(1), Mn1(2), and Mn2. The four Mn1 atoms have a nominal valence 3+ and occupy the bridge sites of the zigzag ferromagnetic chain in the charge exchange (CE) type magnetic order that sets in below the Néel temperature in bulk LCMO. Those Mn1 are further divided into two Mn1(1) and two Mn1(2) sites, by symmetry. The four Mn2 atoms have a nominal valence 4+ and occupy the corner sites of the zigzag ferromagnetic chain.

### B. DFT calculations and downfolding procedure for bulk and nanoclusters

The first step of our study is a DFT calculation of both LCMO bulk and nanoclusters. To this end, we use projected augmented wave (PAW) pseudopotentials with an energy cutoff of 450 eV and performed calculations within a spin-polarized generalized gradient approximation (GGA) [26] as implemented in the Vienna *ab initio* Simulation Package (VASP) [27–30]. The forces on the atoms are converged to less than 0.01 eV/Å. All DFT calculations for bulk LCMO were performed with a $4 \times 2 \times 4k$ mesh. On the other hand, for the nanoclusters we use only the $\Gamma$ point for the $k$-space integration. The structural optimization of the bulk LCMO is performed considering both antiferromagnetic (AFM) CE and ferromagnetic (FM) configurations. We find the AFM CE phase to be lower in energy compared to the FM phase by 45 meV/f.u. [22]. The next step consists in extracting the relevant tight-binding parameters, calculated *ab initio* within DFT, to be used as an input for a low-energy Hamiltonian (see details in Sec. II C) which will be solved within DMFT (see details in Sec. II D). This can be done by employing the downfolding method as implemented in the $N$th-order muffin tin orbital (NMTO) basis [31,32] with potential parameters borrowed from self-consistent linearized muffin-tin orbital (LMTO) [31] calculations. Through the NMTO-downfolding procedure, a low-energy Hamiltonian $H(k)$ involving only Mn $e_g$ Wannier orbitals [33] is constructed in $k$ space by integrating out all other degrees of freedom. The Fourier transformation of $H(k)$ provides the tight-binding parameters. In the following we refer to this structure as $S_{\text{bulk}}$. We use $S_{\text{bulk}}$ to describe bulk manganites within standard DFT+DMFT calculations.

In order to describe nanomanganites on the same footing as the bulk, we employ the following scheme (as explained in Ref. [22]). A cluster of nearly spherical shape having 3 nm diameter is cut out from a large supercell of the bulk crystal structure in monoclinic $P2_1/m$ symmetry, and is then subjected to a full structural optimization. In the following we refer to this structure as $S_{\text{nano}}$. We extract the $MnO_6$ octahedra from the unit cell core region of $S_{\text{nano}}$ and apply various symmetry operations in order to construct a model bulk system, as discussed in Ref. [23]. This procedure takes into account the local oxygen environment around Mn atoms as well as the tilt and rotation connecting two $MnO_6$ octahedra in the core region of the nanocluster. In the following we refer to this structure as $S_{\text{model}}$. Although $S_{\text{nano}}$ does not maintain strict stoichiometry, the constructed $S_{\text{model}}$ is strictly stoichiometric [22,23]. The NMTO-downfolding procedure is then carried out on the self-consistent LMTO calculation for $S_{\text{model}}$, yielding a tight-binding Hamiltonian which contains the information of the structural as well as the electronic changes at the level of one-electron theory that happen upon size reduction. This scheme allows us to describe nanomanganites within standard DFT+DMFT calculations.

The latter approach will provide a reliable description of manganite nanoclusters, under the assumption that the system structure can be described by the hopping parameters extracted from the core of $S_{\text{nano}}$. In order to better understand the effect of size reduction on manganite nanoclusters, in this work we also develop a complementary scheme, which is described in the

following. We use the parameters extracted from the inner core of $S_{\rm nano}$ to construct few-atom nanoclusters of different size. However, due to finite-size effects and the inhomogeneous hopping parameters, the resulting nanoclusters have lower symmetry with respect to $S_{\rm model}$. In particular, the symmetries behind the classification of Mn1(1), Mn1(2), and Mn2 sites (which is exact in both $S_{\rm bulk}$ and $S_{\rm model}$ structures) are partially lifted in the case of finite nanoclusters. In order to take electronic correlations into account, we solve the nanoclusters within the nano-DMFT scheme [34,35], which is suitable to treat electronic correlations in finite-size systems (see details in Sec. II D).

### C. Low-energy effective $e_g + S_{t_{2g}}$ model

The low-energy Hamiltonian describing the manganites is given as [36–38]

$$\mathcal{H} = \sum_{ijmm'} \sum_{\sigma\sigma'} h_{ij,mm'} c^{\dagger}_{im\sigma} c_{jm'\sigma'} - 2\mathcal{J} \sum_{im} \boldsymbol{s}_i S_i + U \sum_{im} n_{im\uparrow} n_{im\downarrow} + \sum_{im<m'} \sum_{\sigma\sigma'} (U' - J\delta_{\sigma\sigma'}) n_{im\sigma} n_{im\sigma'}. \quad (1)$$

In this notation, $c^{(\dagger)}_{im\sigma}$ denotes the annihilation (creation) operator of electrons on site $i$ and orbital $m$, with spin $\sigma$, while $n_{im\sigma} = c^{\dagger}_{im\sigma} c_{im\sigma}$ is the number operator. The one-particle DFT Hamiltonian $h_{ij,mm'}$ is given by the parameters obtained by the NMTO downfolding procedure to the basis of the $e_g$ Wannier orbitals $m,m'$ on sites $i,j$. The on-site Coulomb interaction within the $e_g$ manifold is parametrized in terms of an intraorbital repulsion $U = 5$ eV, a Hund's exchange $J = 0.75$ eV, and an interorbital interaction $U' = U - 2J$ [39–41]. The values of the interaction parameters, taken from the literature [42], represent realistic estimates for manganites. We also consider a Hund's exchange $\mathcal{J}$, coupling the $e_g$ electron spin $\boldsymbol{s}_i = \frac{1}{2} \sum_{\sigma\sigma'} c^{\dagger}_{im\sigma} \boldsymbol{\tau}_{\sigma\sigma'} c_{im\sigma'}$ (with $\tau$ the Pauli matrices) to a (classical) disordered spin $|S_i| = S = 1$, representing the high-spin state of the half-filled $t_{2g}$ manifold ($S_{t_{2g}} = 3/2$). Within DMFT, this term splits the $e_g$ into two parts, parallel and antiparallel to the disordered $t_{2g}$ spin $S$. Instead, here we assume the value $\mathcal{J}S = 1.35$ eV, which was estimated from the $e_g$ band splitting of a spin-polarized DFT calculation [38]. This value is consistent with results of constrained LDA calculations (cLDA), which would yield $J \approx 0.9$–$1$ eV for the Hund's exchange. Recently, the classical spin description of the $t_{2g}$ manifold has been thoroughly revisited [43]. The significant technical improvements in the field of impurity solvers allow the direct treatment of a five-orbital model for the whole Mn $3d$ multiplet, including also spin-flip and pair-hopping terms beyond the density-density Coulomb interaction, which are neglected in the present study [44,45]. Remarkably, in the case of pure $LaMnO_3$, a detailed analysis showed an excellent agreement between a classical spin and a full quantum many-body treatment of the $t_{2g}$ orbitals, e.g., for the $e_g$ spectral functions [43]. Moreover, the estimate obtained for the spin-spin correlations functions $\langle S_z^{e_g} S_z^{t_{2g}} \rangle \approx 0.74$ was found to be consistent with the picture of aligned $e_g$ and $S_{t_{2g}} = 3/2$ spins [43]. In light of these considerations, the restriction to the low-energy model described by Hamiltonian (1) represents a realistic and physically sensible choice to study correlation effects in Mn compounds with a half-filled $t_{2g}$ manifold and partially filled $e_g$ orbitals.

### D. Dynamical mean-field theory with inequivalent Mn atoms in the unit cell

In the following we discuss the technical details for the solution of the many-body Hamiltonian (1) in the framework of DMFT [41,46] for inhomogeneous systems [34,35,47–50]. That is, we solve an auxiliary Anderson impurity problem for each inequivalent Mn site in the unit cell. Moreover, we perform an average over the disordered classical $t_{2g}$ spin $S$ [51]. This procedure yields a local $2 \times 2$ self-energy in the $e_g$ manifold of each of the Mn atoms in the unit cell, while neglecting nonlocal self-energy elements between different Mn atoms. Let us start by discussing the bulk DFT+DMFT calculations, which have been performed on $S_{\rm bulk}$ and $S_{\rm model}$ structures to describe LCMO bulk and nanoscopic (3 nm) clusters. Exploiting the symmetries of the unit cell, the overall computational effort for the bulk amounts to the solution of three auxiliary impurity problems [for Mn1(1), Mn1(2), and Mn2, as defined in Sec. II A] within a DMFT self-consistent scheme, with the corresponding subtraction of three inequivalent double-counting terms in $h_{ij,mm'}$:

$$\Delta^{DC}_{im} = \tilde{U} \left( n^{\rm DFT}_{im} - \frac{1}{2} \right), \quad (2)$$

where $\tilde{U} = U - \frac{5}{3} J$ denotes an averaged interaction and $n^{\rm DFT}_{im}$ are the NMTO orbital occupancies for each of the inequivalent Mn in the unit cell [41,53,54]. In the numerical calculations, we employ a Hirsch-Fye quantum Monte Carlo [55] impurity solver, with a Trotter discretization $\Delta\tau^2 \approx 0.027$ and an inverse temperature $\beta = 20\ {\rm eV}^{-1}$ in the paramagnetic phase.

For the nano-DMFT calculations, we consider the LCMO finite-size nanoclusters shown in Fig. 1, having $N = 46, 20, 8$, and 4 Mn sites, and described by the parameters extracted from $S_{\rm nano}$. As already discussed, the symmetry of the nanoclusters is much lower than in the bulk due to finite-size effects. This leads to many more inequivalent Mn sites than the three [Mn1(1), Mn1(2), and Mn2] of $S_{\rm bulk}$ and $S_{\rm model}$. For example, the $N = 46$ Mn atom cluster contains $N_{\rm ineq} = 23$ inequivalent Mn sites, as it possesses only the inversion symmetry with respect to the center of the cluster. In this case, we need to solve for $i = 1, \ldots, N_{\rm ineq}$ impurity problems, yielding $N_{\rm ineq}$ $2 \times 2$ local self-energy matrices $\Sigma^{ii}_{mm'}$. From these, a new $(2N) \times (2N)$ cluster Green's function is calculated by solving the Dyson equation, enforcing the self-consistency at the level of the whole nanocluster. This scheme has been employed for all the few-atom Mn clusters shown in Fig. 1, taking into account the specific symmetries of each structure. We stress once more that this nano-DMFT approach is different in spirit from that adopted in Ref. [22], in which bulk-DMFT calculations were performed, and the effect of size reduction was considered via the change in tight-binding parameters of $S_{\rm model}$ with respect to $S_{\rm bulk}$. Instead, within nano-DMFT calculations we explicitly take into account the boundary effects of the finite-size nanoclusters constructed with the tight-binding parameters extracted from $S_{\rm nano}$.

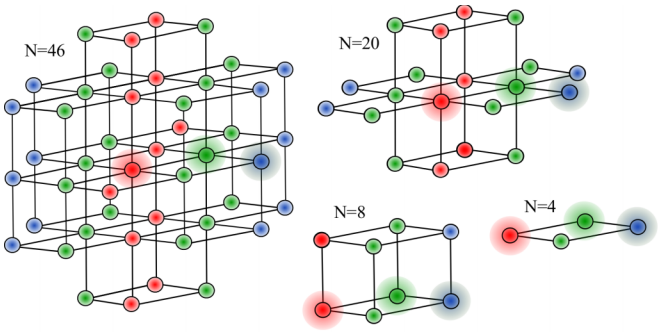


FIG. 1. (Color online) Schematic representation of the Mn sublattice of the few-atom nanoclusters considered, having $N = 46$, 20, 8, and 4 Mn sites. The clusters are built by chopping off atoms from the supercell described by the tight-binding Hamiltonian of $S_{\text{nano}}$. The cluster boundaries correspond to dangling Mn-Mn bonds. The La, Ca, and O octahedra environment is effectively taken into account in the *ab initio* parameters through the downfolding procedure. In each cluster, the red (gray), blue (dark gray), and green (light gray) atoms correspond to Mn1(1), Mn1(2), and Mn2, respectively, according to their classification in the bulk. The highlighted Mn atoms correspond to representative Mn around which the clusters are built.

## III. RESULTS FOR FINITE-SIZE LCMO NANOCLUSTERS

### A. Spectral properties

In the following we discuss the spectral properties of the nanoclusters shown in Fig. 1. The DMFT spectral functions are shown in Fig. 2, for three representative Mn1(1), Mn1(2), and Mn2 sites, following the bulk classification. Even though Mn sites of each class are no longer equivalent, and local observables display quantitative changes from site to site, the data analysis shows that one can still identify a common qualitative behavior for Mn sites within each class. At the outset, we notice that the size reduction has profound consequences on the electronic structure of the LCMO nanoclusters, in the sense that the metallic character decreases gradually in moving from $N = 46$ to 4. In the extreme case of $N = 4$, the system is in an insulating state even at the high temperature considered here ($\beta = 20$ eV$^{-1}$), reflecting the strong quantum confinement effects induced upon size reduction (bottom row of Fig. 2). The observed metal-to-insulator transition is accompanied by a strong enhancement of the charge disproportionation between $Mn^{3+}$ and $Mn^{4+}$, as well as an overall enhancement of the orbital polarization between two $e_g$ orbitals, $3z^2 - r^2$ and $x^2 - y^2$. This means that the charge is almost completely on Mn1(1) and Mn1(2), with mostly $3z^2 - r^2$ character, and as

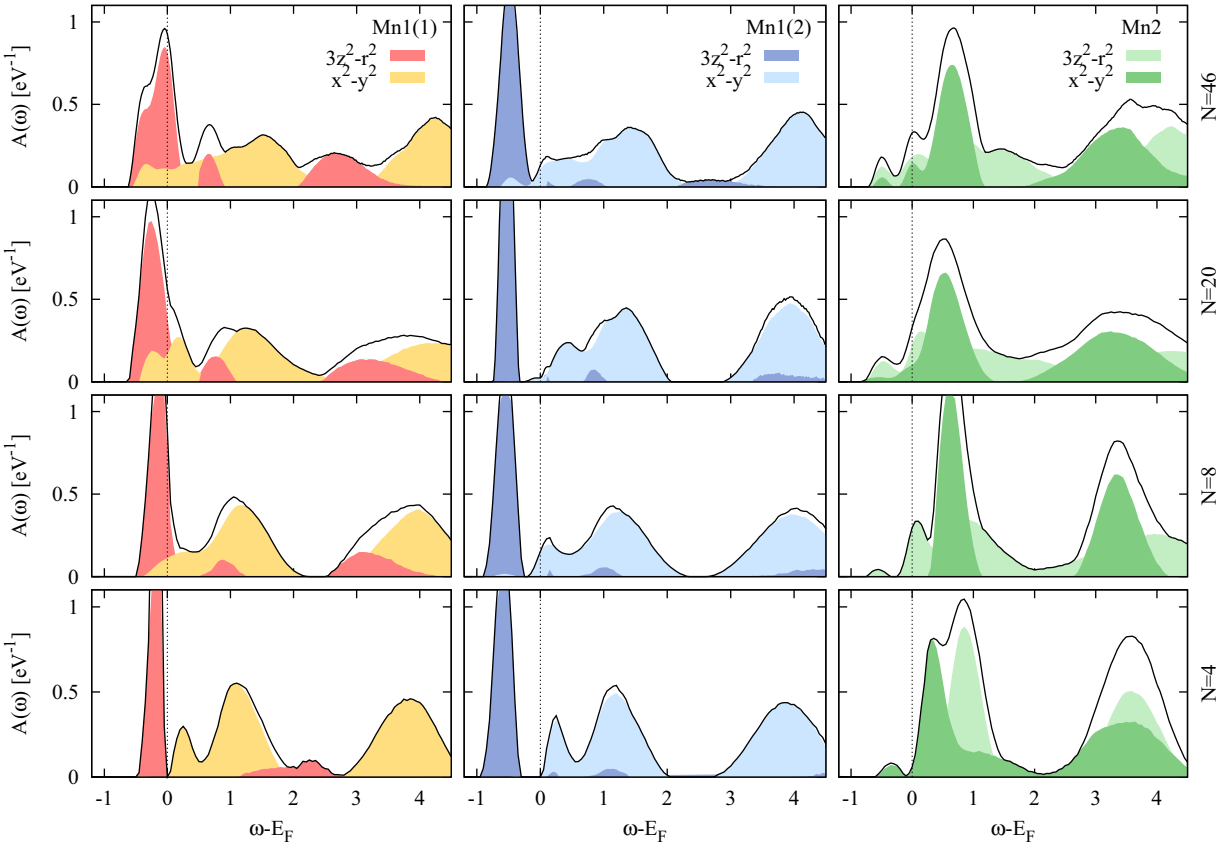


FIG. 2. (Color online) Evolution of the spectral properties of the nanoclusters, shown in Fig. 1, described by the tight-binding parameters of $S_{\text{nano}}$. Each row shows the spectral function $A(\omega)$ for a cluster having $N$ Mn atoms. The red (gray), blue (dark gray), and green (light gray) lines correspond to representative Mn1(1), Mn1(2), and Mn2 atoms, respectively, indicated by shaded spheres in the nanoclusters shown in Fig. 1. The dark and light filled curves in each panel denote the contributions from the $3z^2 - r^2$ and $x^2 - y^2$ orbitals, while the black solid line denotes the on-site spectral density of the $e_g$ manifold. A metal-to-insulator transition (MIT) upon decreasing cluster size, due to quantum confinement effect, is evidenced accompanied by an enhancement of the charge and orbital order.

a consequence Mn2 sites are almost empty. The enhancement of the orbital polarization upon decreasing cluster size is stronger for Mn1(1), which are located at the core of the clusters and experience the localization of the $e_g$ states due to quantum confinement. Instead, all Mn1(2) sites are located at the surface of the clusters (i.e., with maximum number of dangling bonds) and have a nearly insulating and almost fully orbitally polarized spectral function irrespective of cluster size.

It is interesting to compare these results with the ones obtained for bulk and nano LCMO using the parameters of $S_{\rm bulk}$ and $S_{\rm model}$, respectively. In bulk LCMO, the orbital polarization is almost complete for Mn1 and zero for Mn2, and the system displays also a strong charge disproportionation, resulting in an insulating state. As was shown for a nanocluster of 3 nm diameter [22], upon size reduction both the charge disproportionation between Mn1 and Mn2 atoms and the orbital polarization at the Mn1 sites decrease considerably compared to the bulk, leading to metallicity. This effect is induced by the structural distortion associated with size reduction. In the present work, we find instead that further reducing the size to few-atom nanoclusters (i.e., from $N = 46$ to 4 Mn sites) the effect is reversed: as quantum confinement effect comes into play, and the $e_g$ orbitals become more and more localized, the charge disproportionation and orbital polarization increase, and become almost complete in the $N = 4$ nanocluster.

### B. Charge and orbital order

In order to quantify the effects of size reduction inferred from the analysis of the spectral functions of representative Mn atoms in each cluster, in the following we describe charge and orbital correlations considering cluster-averaged quantities. Let us define the local occupation $n_i$ and the local orbital polarization $\Delta p_i$ (between $x^2 - y^2$ and $3r^2 - z^2$ orbitals) on Mn site $i$ as

$$n_i = \frac{1}{2}\sum_S \sum_{m\sigma} n^S_{im\sigma},$$
$$\Delta p_i = \frac{1}{2}\sum_S \sum_{m\sigma} n^S_{im\sigma}(-1)^m, \tag{3}$$

where the average over $S$ takes into account the two possible configurations of the classical $t_{2g}$ spin. Hence, we define the cluster-averaged quantities

$$\langle \Delta n \rangle = \frac{1}{N_{\rm Mn1}}\sum_{i\in {\rm Mn1}} n_i - \frac{1}{N_{\rm Mn2}}\sum_{i\in {\rm Mn2}} n_i,$$
$$\langle \Delta p_\alpha \rangle = \frac{1}{N_\alpha}\sum_{i\in\alpha} \Delta p_i. \tag{4}$$

In particular, $\langle \Delta n \rangle$ is the charge disproportionation between Mn1 and Mn2 atoms, averaged over the nanocluster, while $\langle \Delta p_\alpha \rangle$ is the orbital polarization averaged over all Mn sites in the nanocluster belonging to Mn kind $\alpha$. Note that in Eq. (4), the occupation $n_i$ and the polarization $p_i$ for different Mn sites $i$ (even for those belonging to the same Mn kind $\alpha$) are in general inequivalent because of the lower symmetry of the finite nanoclusters constructed from $S_{\rm nano}$, with respect to the bulk models described by $S_{\rm bulk}$ or $S_{\rm model}$.

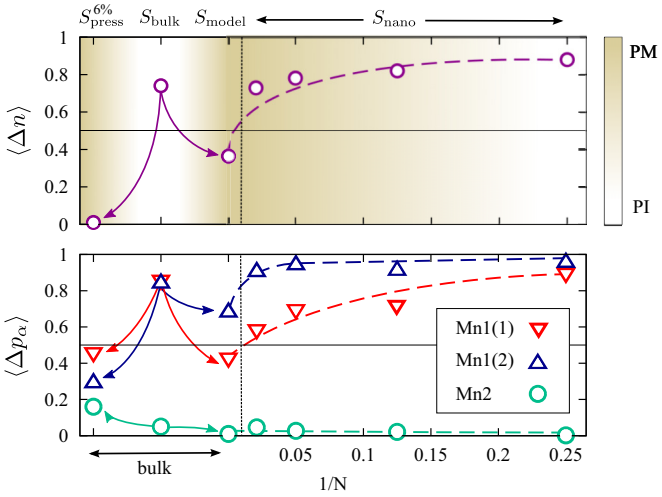


FIG. 3. (Color online) Cluster-averaged charge order $\langle \Delta n \rangle$ (upper panel) and orbital polarization $\langle \Delta p_\alpha \rangle$ (lower panel) of LCMO bulk and clusters. On the right-hand side of each pane we show the nano-DMFT results obtained for the finite-size clusters built with the parameters of $S_{\rm nano}$, as a function of the (inverse) number of the Mn atoms in the cluster. On the left-hand side of each panel we also show the DFT+DMFT results obtained within the calculations of Ref. [22] for the bulk model $S_{\rm model}$ (applicable for 3 nm diameter cluster containing about 200 Mn atoms) and on bulk LCMO $S_{\rm bulk}$. Those are compared to additional DFT+DMFT result for $S_{\rm press}$, corresponding to the bulk under the application of hydrostatic pressure, resulting in 6% volume reduction. The light brown (light gray) shade in the upper panel represents the transitions between PI and PM phases. Arrows and dashed lines are a guide to the eye.

The cluster-averaged $\langle \Delta n \rangle$ and $\langle \Delta p_\alpha \rangle$ are shown on the right-hand side of each panel in Fig. 3 (indicated by the label $S_{\rm nano}$) as a function of the (inverse) number of the Mn atoms in the cluster. For comparison, on the left-hand side of each panel the results obtained in Ref. [22] within DFT+DMFT calculation performed on the bulk nanomodel $S_{\rm model}$ (applicable to 3 nm diameter cluster containing about 200 Mn atoms) are also shown. As a general trend, the charge order and orbital polarization are found to be the largest for the smallest cluster and decrease upon increasing the cluster size. In particular, $\Delta n$ shows a smooth reduction with increasing system size from a value close to $\langle \Delta n \rangle \approx 0.9$ for $N = 4$, corresponding to the limit in which the Mn2 sites are completely empty, to $\langle \Delta n \rangle \approx 0.7$ for $N = 46$. Those values can be compared to $\Delta n \approx 0.35$ found for $S_{\rm model}$. A similar behavior is found for the averaged orbital polarization, although the values of $\langle \Delta p_\alpha \rangle$ seem to be somewhat dependent on the system shape and symmetry, especially for the smaller nanoclusters considered here. However, in general the orbital polarization of the Mn1 atoms tends to decrease, by increasing cluster size, while that for the (almost empty) Mn2 atoms is always negligible. A more careful analysis (not shown) reveals that the site-dependent $\Delta p_i$ is not homogeneous within the cluster. In particular, Mn atoms located at the surface of the cluster display, besides sharper spectral structures, also a stronger orbital polarization than the Mn atoms located at the core of the cluster.

In this respect, we can also compare the above results to those obtained from the DFT+DMFT calculations of Ref. [22] for the bulk. We find that both the charge order $\langle \Delta n \rangle$ and the orbital polarization $\langle \Delta p_\alpha \rangle$ are strongly enhanced for $S_{\rm bulk}$ with respect to the 3 nm cluster size described by $S_{\rm model}$, and are accompanied by a metal-to-insulator transition. The previous observations can be summarized in the following scenario: Starting from the smallest size cluster and upon progressively increasing the system size, one encounters an insulator-to-metal transition in few-atom nanoclusters, which is driven by a weakening of quantum confinement effects and charge-orbital correlations, and consequent delocalization of the $e_g$ orbitals. With increasing the size of the nanocluster, the system smoothly evolves towards the results obtained for the bulk nanomodel, which is metallic due to the weak structural distortions included in the parameters of $S_{\rm model}$. On the other hand, bulk LCMO $S_{\rm bulk}$ is strongly distorted. The structural distortions lead to the enhancement of charge-orbital order and drive the system across a second metal-to-insulator transition between $S_{\rm model}$ (3 nm) and $S_{\rm bulk}$ (bulk) [22].

In order to disentangle the effects induced by nanostructuring from those related to the volume reduction of the unit cell, we also consider bulk LCMO under applied hydrostatic pressure $S_{\rm press}$. The tight-binding parameters of $S_{\rm press}$ are obtained *ab initio* from a DFT calculation under pressure, through the downloading procedure described in Sec. II B for the bulk. For this calculation, we consider the value of the hydrostatic pressure yielding the same volume reduction of the unit cell, i.e., 6%, as for the 3 nm nanocluster. Experimentally, a volume reduction of 6% can be obtained, for the parent compound $LaMnO_3$, by applying a pressure of about 10 GPa [56]. We compare the DFT+DMFT results obtained for $S_{\rm model}$ and for $S_{\rm press}$ (denoted in Fig. 3 by the label $S^{6\%}_{\rm press}$) and we find that in both cases the system is metallic. However, the effects of hydrostatic pressure and the size reduction are substantially different. In particular, we find for $S_{\rm press}$ a negligible charge disproportionation between Mn1 and Mn2, and an overall reduction of the orbital polarization. This is also shown in detail in Table I, where we compare the orbital-resolved occupations of $S_{\rm press}$ and $S_{\rm model}$. While the results obtained within DFT for the two systems are rather similar, the effect of electronic correlations within DMFT strongly enhances charge and orbital order in $S_{\rm model}$, while it has a much weaker effect in $S_{\rm press}$. Hence, we can conclude that the system under hydrostatic pressure is much deeper into the metallic phase compared to a 3 nm cluster, and that the different behavior of systems with the same volume is determined by their different structural distortions, which are specific to the way the volume reduction is achieved.

TABLE I. Orbital DFT+DMFT occupancies for the three inequivalent Mn atoms in the unit cell of $S_{\rm model}$ and $S_{\rm press}$. In parentheses we give the corresponding occupancies for the one-particle low-energy DFT Hamiltonian without the effect of DMFT correlations, which strongly enhance the charge-orbital order. Both the orbital polarization in Mn1 atoms and the charge disproportionation between Mn1 and Mn2 atoms are more pronounced for the nanomodel $S_{\rm model}$ than for the pressurized bulk system $S_{\rm press}$.

| | Pressure 6% | | Nanomodel | |
|---|---|---|---|---|
| | $3z^2-r^2$ | $x^2-y^2$ | $3z^2-r^2$ | $x^2-y^2$ |
| Mn1(1) | 0.52 (0.39) | 0.06 (0.11) | 0.52 (0.31) | 0.09 (0.20) |
| Mn1(2) | 0.36 (0.34) | 0.07 (0.13) | 0.72 (0.38) | 0.04 (0.19) |
| Mn2 | 0.33 (0.31) | 0.17 (0.21) | 0.16 (0.21) | 0.16 (0.25) |

### C. Site- and orbital-selective Mott transition driven by applied gate voltage

The interesting insulator-to-metal-to-insulator series of transitions observed in LCMO upon size reduction originates from a complex interplay between quantum confinement effects and the (weakening of the) structural distortions occurring upon size reduction from the bulk LCMO to the 3 nm nanocluster. As the onset of the peculiar charge- and orbital-ordered state found in the bulk LCMO relies on the balance between $Mn^{3+}$ and $Mn^{4+}$, it is interesting to study the effect of electron doping for the nanoclusters. A change in the number of carriers without changing the chemical composition of the system can be achieved by the application of an external gate voltage $V_g$. In this section, we investigate this issue through DMFT calculations considering the clusters with $N = 46$ and 4 Mn atoms. We consider the limiting case where there is only an infinitesimally small tunneling contact with the environment, so that the we can account for the gate voltage by changing the DMFT chemical potential. We neglect the effect of doping on the DFT effective potential, as in the virtual crystal approximation [57].

In Fig. 4 we show the orbitally resolved spectral weight at the Fermi energy $\overline{A(E_F)}$ (averaged over a unit energy window $\sim T$) as calculated from the Green's function at imaginary time $\tau = \beta/2$, and the occupations of the two $e_g$ orbitals for representative Mn sites of $S_{\rm nano}$. The value $V_g = 0$ corresponds to the results in the previous sections and to an average cluster occupation $\langle n \rangle = 0.5$ electrons in the $e_g$ orbitals. We recall that, in this configuration, Mn1 sites display a strong orbital polarization, while Mn2 sites are almost empty. Upon changing $V_g$, we increase the number electrons in the LCMO cluster (electron doping). When the low-lying $e_g$ orbital (e.g., the $3z^2 - r^2$ in the case of Mn1) on a Mn site becomes half filled, strong electronic correlations drive an orbital-selective metal-to-insulator transition, with the opening of a Mott gap, while the other orbital is still metallic. Such an orbital-selective Mott transition has been reported before for the Hubbard model, originating from different bandwidth for different orbitals [58–65], due to the band degeneracy lifting [66], and can be driven by Hund's coupling or crystal field splitting [67]. Evidence for an orbital-selective Mott transition has also been observed for other materials [68–70]. The charge disproportionation between $Mn^{3+}$ and $Mn^{4+}$ also results in a strong site-selective character of the transition; i.e., Mn1 sites enter the orbital-selective phase at a lower value of $V_g$ with respect to Mn2. Site-selective behavior of similar kind has also been reported recently for bulk systems [71,72]. In our case, we have one insulating orbital which is integer filled ($n = 1$), but neither the occupation of the other (metallic) orbital nor the cluster average electron density is integer. One possible interpretation of this orbital- and site-selective Mott transition is associated with the role of the Hund's exchange coupling to

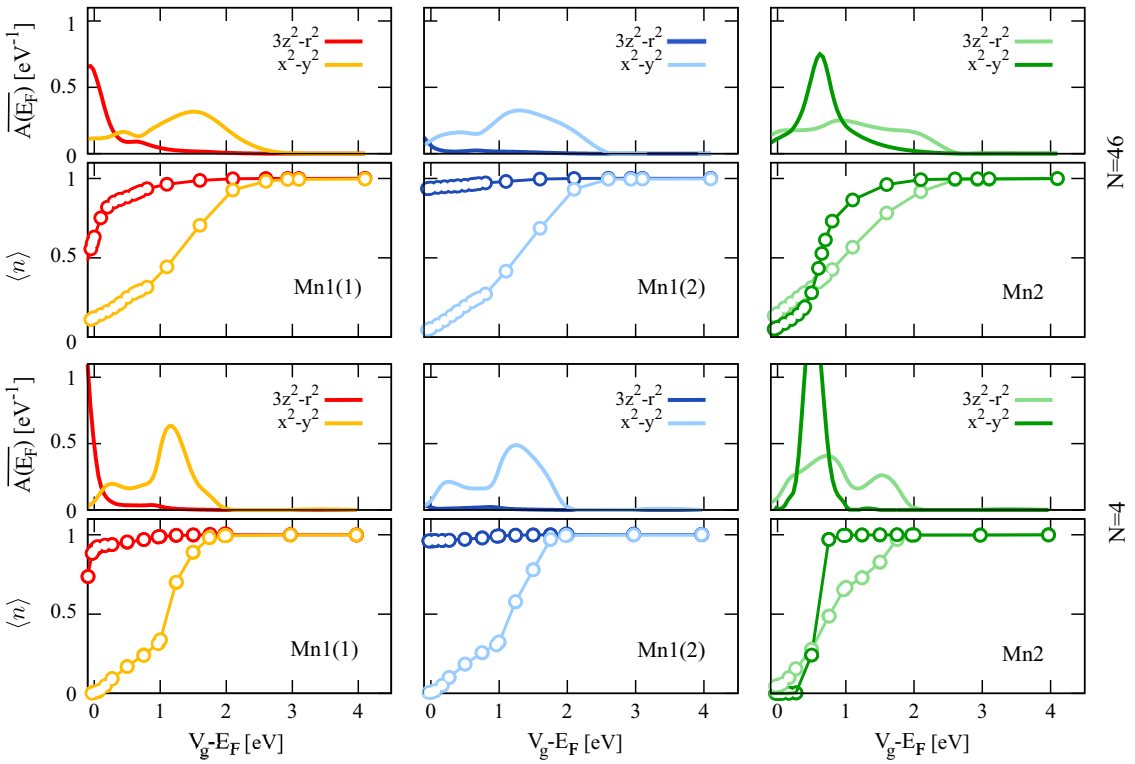


FIG. 4. (Color online) Evolution of the spectral weight at the Fermi energy $\overline{A(E_F)}$ (averaged over an energy window $\sim T$) and of the orbitally resolved occupation with gate voltage $V_g$ (electron doping) for the representative Mn sites of the $N = 46$ (upper panels) and $N = 4$ (lower panels) clusters. The red (gray), blue (dark gray), and green (light gray) curves correspond to representative Mn1(1), Mn1(2), and Mn2 atoms, respectively, while the light and dark colors denote $3z^2 - r^2$ and $x^2 - y^2$ states. The gate voltage $V_g$ drives an orbital-selective Mott transition, which becomes sharper upon decreasing the system size.

the $t_{2g}$ spins. A filling of one electron in an orbital thus means that all states with spin parallel to the $t_{2g}$ spins are occupied, while those with opposite spin are empty.

In the case of the $N = 46$ Mn sites nanocluster, we find that *all* Mn1 sites enter the orbital-selective Mott phase almost simultaneously, at $V_g \approx 1$ eV, as indicated by the spectral weight $A(E_F) = 0$ and a diverging self-energy (not shown) for both Mn1(1) and Mn1(2) (see upper panels in Fig. 4). In fact, despite the differences given by the local crystal field environment, in $S_{\text{nano}}$ Mn1(1) and Mn1(2) sites are more similar to each other than in $S_{\text{bulk}}$, due to the weakening of the structural distortions upon size reduction. For values $1 \lesssim V_g \lesssim 2$ eV the system is in a site- and orbital-selective phase, until also the low-lying $e_g$ orbital of Mn2 sites ($x^2 - y^2$) turns insulating. Upon further increasing $V_g$ the system becomes more homogeneous, and all Mn sites display similar occupations in the metallic $e_g$ states. Eventually, the whole nanocluster enters a Mott phase, and above $V_g \approx 2.6$ eV we do not find any variation in the occupation, an indication of the fact that the chemical potential lies within the Mott gap.

In the case of the $N = 4$ Mn sites nanocluster we find a similar behavior, with some important differences. Due to the quantum confinement, at $V_g = 0$ the charge is almost completely localized at the Mn1 sites (which are almost half filled and exhibit a strong orbital polarization. Moreover, most of the charge carriers introduced in the cluster localize in the low-lying Mn2 $e_g$ orbitals, which rapidly fill up towards half filling. As a result, site selectivity is lost, and the whole cluster enters the orbital-selective phase at $V_g \approx 1$ eV. Upon further increasing $V_g$, also the other metallic orbitals become half filled, and the cluster eventually turns insulating at $V_g \approx 2$ eV.

In general, we observe that, upon decreasing the cluster size, the orbital-selective Mott transition is found at a smaller value of $V_g$. The transition also appears to be sharper upon changing $V_g$. This can be understood by considering the more localized nature of the $e_g$ orbitals and the enhanced orbital polarization observed for smaller cluster sizes. This effect is important in view of possible applications, as it shows that, for an appropriate system size, half-doped LCMO manganite nanoclusters can be driven across a metal-to-insulator by applying an external gate voltage.

## IV. CONCLUSIONS

We investigated the effects of size reduction on the charge and orbital order in the LCMO mixed valence manganite within the DFT+DMFT framework. As was shown before [22], the size reduction from bulk to a 3 nm nanocluster weakens the distortions of the bulk crystal structure and induces an insulator (bulk)–to–metal (3 nm) transition in the high-temperature paramagnetic phase, along with a weakening of charge and orbital disproportionation. Here, we extend the analysis by considering nanoclusters of just a few atoms. Upon reducing the system size we observe the opposite trend: driven by the quantum confinement, there is a second

metal (3 nm)–to–insulator (a few atoms) transition and an enhancement of both charge and orbital disproportionation. We also investigated the effect of electron doping on the few-atom nanoclusters by applying an external gate voltage. We observe an orbital-selective Mott transition at a critical value of the gate voltage which corresponds to an integer filling of only an individual $e_g$ orbital. The orbital-selective nature of the transition is a direct consequence of the orbital polarization and the strong Hund's exchange splitting. At the same time, the strong charge disproportionation between $Mn^{3+}$ and $Mn^{4+}$ sites induces also a site-selective character, with different Mn kinds turning insulating at different values of the gate voltage.

Our theoretical prediction of a reentrant insulator-to-metal-to-insulator transition and the reported gate voltage control calls for further experiments. Technical applications are discernible since these two control parameters should allow us to fine-tune LCMO nanoclusters to the verge of a Mott transition. In this situation the smallest changes in temperature, voltage, magnetic field, etc., can trigger a gigantic change in the conductance.

## ACKNOWLEDGMENTS

We acknowledge financial support from the Austrian Science Fund (FWF) through I-610-N16 (A.V.), the Deutsche Forschungsgemeinschaft FOR 1346 (G.S.), and the European Research Council under the European Union's Seventh Framework Program FP7/ERC through Grant Agreements No. 306447 (A.V., K.H.) and No. 240524 (A.V.). H.D. and T.S.D. would like to acknowledge the Department of Science and Technology, India, for support. The numerical calculations were performed on the Vienna Scientific Cluster (VSC).

[1] G. M. Jonker and J. H. van Santen, Physica **16**, 337 (1950).
[2] R. von Helmolt, J. Wecker, B. Holzapfel, L. Schultz, and K. Samwer, Phys. Rev. Lett. **71**, 2331 (1993).
[3] S. Jin, T. H. Tiefel, M. McCormack, R. A. Fastnacht, R. Ramesh, and L. H. Chen, Science **264**, 413 (1994).
[4] R. M. Kusters, S. Singelton, D. A. Keen, R. McGreevy, and W. Hayes, Physica B **155**, 362 (1989).
[5] P. Schiffer, A. P. Ramirez, W. Bao, and S-W. Cheong, Phys. Rev. Lett. **75**, 3336 (1995).
[6] E. O. Wollan and W. C. Koehler, Phys. Rev. **100**, 545 (1955).
[7] H. Kuwahara, Y. Tomioka, A. Asamitsu, Y. Moritomo, and Y. Tokura, Science **270**, 961 (1995).
[8] D. P. Kozlenko, Z. Jirák, I. N. Goncharenko, and B. N. Savenko, J. Phys.: Condens. Matter **16**, 5883 (2004).
[9] A. Asamitsu, Y. Tomioka, H. Kuwahara, and Y. Tokura, Nature (London) **388**, 50 (1997).
[10] T. Sarkar, A. K. Raychaudhuri, and T. Chatterji, J Appl. Phys. Lett. **92**, 123104 (2008).
[11] T. Sarkar, B. Ghosh, A. K. Raychaudhuri, and T. Chatterji, Phys. Rev. B **77**, 235112 (2008).
[12] S. M. Zhou, S. Y. Zhao, Y. Q. Guo, J. Y. Zhao, and L. Shi, J. Appl. Phys. **107**, 033906 (2010).
[13] P. M. Chowdhury, B. Ghosh, A. K. Raychaudhuri, S. D. Kaushik, and V. Siruguri, J. Nanopart. Res. **15**, 1585 (2013).
[14] G. Iniama, P. de la Presa, J. M. Alonso, M. Multigner, B. I. Ita, R. Cortés-Gil, M. L. Ruiz-González, A. Hernando, and J. M. Gonzalez-Calbet, J. Appl. Phys. **116**, 113901 (2014).
[15] S. S. Rao, S. Tripathi, D. Pandey, and S. V. Bhat, Phys. Rev. B **74**, 144416 (2006).
[16] K. S. Bhagyashree and S. V. Bhat, J. Appl. Phys. **117**, 17D514 (2015).
[17] L. R. Goveas, K. N. Anuradha, K. S. Bhagyashree, and S. V. Bhat, J. Appl. Phys. **117**, 17E111 (2015).
[18] T. Sarkar, P. K. Mukhopadhyay, A. K. Raychaudhuri, and S. Banerjee, J. Appl. Phys. **101**, 124307 (2007).
[19] S. S. Rao, K. N. Anuradha, S. Sarangi, and S. V. Bhat, Appl. Phys. Lett. **87**, 182503 (2005).
[20] T. Zhang and M. Dressel, Phys. Rev B **80**, 014435 (2009).
[21] Z. Jirák, E. Hadová, O. Kaman, K. Knížek, M. Maryško, E. Pollert, M. Dlouhá, and S. Vratislav, Phys. Rev. B **81**, 024403 (2010).
[22] H. Das, G. Sangiovanni, A. Valli, K. Held, and T. Saha-Dasgupta, Phys. Rev. Lett. **107**, 197202 (2011).
[23] See Supplemental Material of Ref. [22] for details on the crystal structures as well as on construction of the model structure.
[24] F.-L. Tang, Y.-X. Hu, W.-J. Lu, K. Chu, Y.-D. Feng, C.-H. Wu, and M. Xu, J. Magn. Magn. Mater. **333**, 8 (2013).
[25] C. Zener, Phys. Rev. **82**, 403 (1951).
[26] J. P. Perdew, K. Burke, and M. Ernzerhof, Phys. Rev. Lett. **77**, 3865 (1996); **78**, 1396 (1997).
[27] G. Kresse and J. Hafner, Phys. Rev. B **47**, 558 (1993).
[28] G. Kresse and J. Hafner, Phys. Rev. B **49**, 14251 (1994).
[29] G. Kresse and J. Furthmüller, Comput. Mater. Sci. **6**, 15 (1996).
[30] G. Kresse and J. Furthmüller, Phys. Rev. B **54**, 11169 (1996).
[31] O. K. Andersen, Phys. Rev. B **12**, 3060 (1975).
[32] O. K. Andersen and T. Saha-Dasgupta, Phys. Rev. B **62**, R16219 (2000).
[33] G. H. Wannier, Phys. Rev. **52**, 191 (1937).
[34] A. Valli, G. Sangiovanni, O. Gunnarsson, A. Toschi, and K. Held, Phys. Rev. Lett. **104**, 246402 (2010).
[35] A. Valli, G. Sangiovanni, A. Toschi, and K. Held, Phys. Rev. B **86**, 115418 (2012).
[36] K. Held and D. Vollhardt, Phys. Rev. Lett. **84**, 5168 (2000).
[37] K. H. Ahn and A. J. Millis, Phys. Rev. B **61**, 13545 (2000).
[38] A. Yamasaki, M. Feldbacher, Y.-F. Yang, O. K. Andersen, and K. Held, Phys. Rev. Lett. **96**, 166401 (2006).
[39] This relation holds in the case of degenerate orbitals, with the Hamiltonian being invariant under orbital rotations [40]. However, it is considered physically sensible also when the symmetry is fulfilled only approximately [41], e.g., if the $e_g$ orbitals are split by the Jahn-Teller crystal field.
[40] A. M. Oles`, Phys. Rev. B **28**, 327 (1983).
[41] K. Held, Adv. Phys. **56**, 829 (2007).
[42] J.-H. Park, C. T. Chen, S-W. Cheong, W. Bao, G. Meigs, V. Chakarian, and Y. U. Idzerda, Phys. Rev. Lett. **76**, 4215 (1996).
[43] A. Flesch, E. Gorelov, E. Koch, and E. Pavarini, Phys. Rev. B **87**, 195141 (2013).
[44] N. Parragh, A. Toschi, K. Held, and G. Sangiovanni, Phys. Rev. B **86**, 155158 (2012).
[45] E. Gull, A. J. Millis, A. I. Lichtenstein, A. N. Rubtsov, M. Troyer, and P. Werner, Rev. Mod. Phys. **83**, 349 (2011).

[46] A. Georges, G. Kotliar, W. Krauth, and M. Rozenberg, Rev. Mod. Phys. **68**, 13 (1996).
[47] M. Potthoff and W. Nolting, Phys. Rev. B **59**, 2549 (1999).
[48] M. Snoek, I. Titvinidze, C. Töke, K. Byczuk, and W. Hofstetter, New J. Phys. **10**, 093008 (2008).
[49] I. Titvinidze, A. Schwabe, N. Rother, and M. Potthoff, Phys. Rev. B **86**, 075141 (2012).
[50] A. Valli, T. Schäfer, P. Thunström, G. Rohringer, S. Andergassen, G. Sangiovanni, K. Held, and A. Toschi, Phys. Rev. B **91**, 115115 (2015).
[51] Note that in general the Hund's exchange $\mathcal{J}$ entails effective nonlocal (short-range) magnetic correlations between different Mn atoms, which are neglected in DMFT. However, it has been shown [52] that those correlations are less important at high temperature as well as for lattice structures with high coordination, and DMFT provides reliable results. Also note that the average of an Ising spin $S = \pm 1$ yields the same DMFT Green's function for the paramagnetic phase as the angular average of a classical spin with $|\vec{S}| = 1$.
[52] D. Rotter, A. Valli, G. Sangiovanni, and K. Held, Eur. Phys. J. B **86**, 68 (2013).
[53] V. I. Anisimov, J. Zaanen, and O. K. Andersen, Phys. Rev. B **44**, 943 (1991).
[54] M. T. Czyżyk and G. A. Sawatzky, Phys. Rev. B **49**, 14211 (1994).
[55] J. E. Hirsch and R. M. Fye, Phys. Rev. Lett. **56**, 2521 (1986).
[56] I. Loa, P. Adler, A. Grzechnik, K. Syassen, U. Schwarz, M. Hanfland, G. Kh. Rozenberg, P. Gorodetsky, and M. P. Pasternak, Phys. Rev. Lett. **87**, 125501 (2001).
[57] L. Nordheim, Ann. Phys. (Leipzig) **9**, 607 (1931).
[58] A. Liebsch, Europhys. Lett. **63**, 97 (2003).
[59] A. Koga, N. Kawakami, T. M. Rice, and M. Sigrist, Phys. Rev. Lett. **92**, 216402 (2004).
[60] R. Arita and K. Held, Phys. Rev. B **72**, 201102(R) (2005).
[61] L. de Medici, A. Georges, and S. Biermann, Phys. Rev. B **72**, 205124 (2005).
[62] C. Knecht, N. Blümer, and P. G. J. van Dongen, Phys. Rev. B **72**, 081103(R) (2005).
[63] M. Ferrero, F. Becca, M. Fabrizio, and M. Capone, Phys. Rev. B **72**, 205126 (2005).
[64] E. Jakobi, N. Blümer, and P. G. J. van Dongen, Phys. Rev. B **80**, 115109 (2009); **87**, 205135 (2013).
[65] H. Lee, Y.-Z. Zhang, H. O. Jeschke, R. Valenti, and H. Monien, Phys. Rev. Lett. **104**, 026402 (2010).
[66] L. de' Medici, S. R. Hassan, M. Capone, and X. Dai, Phys. Rev. Lett. **102**, 126401 (2009).
[67] P. Werner and A. J. Millis, Phys. Rev. Lett. **99**, 126405 (2007).
[68] V. Anisimov, I. A. Nekrasov, D. E. Kondakov, T. M. Rice, and M. Sigrist, Eur. Phys. J. B **25**, 191 (2002).
[69] M. Neupane, P. Richard, Z.-H. Pan, Y.-M. Xu, R. Jin, D. Mandrus, X. Dai, Z. Fang, Z. Wang, and H. Ding, Phys. Rev. Lett. **103**, 097001 (2009).
[70] R. Yu and Q. Si, Phys. Rev. Lett. **110**, 146402 (2013).
[71] H. Park, A. J. Millis, and C. A. Marianetti, Phys. Rev. Lett. **109**, 156402 (2012).
[72] M. Karolak, M. Izquierdo, S. L. Molodtsov, and A. I. Lichtenstein, Phys. Rev. Lett. **115**, 046401 (2015).